2024 IEEE International Conference on Robotics and Automation (ICRA 2024)
May 13-17, 2024. Yokohama, Japan

Underwater Volumetric Mapping using Imaging Sonar and Free-Space Modeling Approach

António J. Oliveira, Bruno M. Ferreira, Nuno A. Cruz

***Abstract*— Lack of information and perceptual ambiguity are key problems in sonar-based mapping applications. We propose a technique for mapping of underwater environments, building on the finite, positive, sonar beamwidth. Our approach models the free-space covered by each emitted acoustic pulse, employing volumetric techniques to create grid-based submaps of the unoccupied water volumes through images collected from imaging sonars. A representation of the occupied space is obtained by exploration of the free-space frontier. Special attention is given to acoustic image preparation and segmentation. Experimental results are provided based on real data collected from a dam shaft scenario.**

I. Introduction

Building accurate representations of the environment is central in many underwater operations. Obtaining such representation can be the outcome of an underwater mission or can be a mean to accomplish a more complex task. Applications range from inspection or bathymetric surveys to exploration, which are often undertaken through autonomous or remotely operated vehicles that can withstand the demanding environment conditions. Sonars are commonly preferred for mapping purposes when compared to electromagnetic-based or optical alternatives, due to the extended sensing range and better immunity to surrounding fluid characteristics. In this work, we address the sonar perceptual ambiguity problem raised by the non-zero beam aperture, which, by covering a large water volume, brings additional challenges in accurately locating the reflection point of recorded acoustic echoes and represents a source of mapping uncertainty. This imposes additional challenges compared to their laser-based counterparts, commonly employed in terrestrial applications, as the ambiguity to discriminate the reflecting surface is much higher.

Occupancy grid-based approaches are one the most widespread solutions for underwater mapping applications. Sonar-based approaches employ the acoustic returns from environmental elements for updating the occupancy probability of the insonified regions. In [1], sonar features are extracted through adaptive thresholding and clustering to build a Gaussian process three-dimensional occupancy map of submerged structures. Sonar data segmentation is undertaken in [2] resorting to the Constant False Alarm Rate (CFAR) detector [3] to identify free and occupied volumes in the surrounding environment. The work in [4] explores the application of Mechanical Scanning Imaging Sonars (MSISs) for three-dimensional underwater reconstruction applications using the Octomap framework [5] and clustering-based sonar interest data extraction, assessing mapping performance in different scenarios. A volumetric submapping technique using multibeam sonar scans is introduced in [6]. Resorting to the Octomap framework and a factor graph approach, pairwise submap alignment constraints are generated by means of scan matching and used to correct navigation drift and improve map accuracy. The authors in [7] expand on this algorithm and propose an approach for building global deformable virtual occupancy maps, focusing on correcting globally accumulated drift via loop closures using the local submaps.

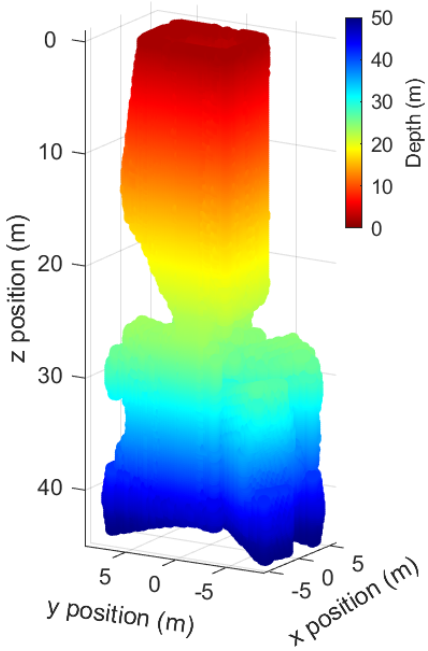

Fig. 1: Illustration of the occupied surface map created for the testing environment, with depth-based color coding.

However, sonar-based underwater mapping solutions are hampered by a lack of data and a decline in the quality of the collected information, due to the inability to accurately locate the reflection point of recorded acoustic echoes. In opposition to other range sensors, sonar scans do not portray precise cross-sections of the two dimensional scanning plane, as the wider sonar beamwidth covers a larger water volume. In laser-based sensors, for example, the beamwidth is usually

This work is financed by National Funds through the Portuguese funding agency, FCT - Fundação para a Ciência e a Tecnologia, within project UIDP/50014/2020 (DOI 10.54499/UIDP/50014/2020). The first author is also supported by the Portuguese Foundation for Science and Technology through the Ph.D. scholarship 2021.08065.BD.

Authors are with INESC TEC, Faculty of Engineering, University of Porto, Porto, Portugal antonio.ventura@fe.up.pt

neglected for mapping purposes, as it is typically lower than $1°$. In the case of the sonar considered in this work, the emitted acoustic pulse presents much larger horizontal and vertical apertures, of $3°$ and $35°$, respectively.

To address this issue, a strand of solutions in literature has focused on multi-sensor approaches. In [8] a two-dimensional grid mapping approach employing two different sonar types is introduced. In their work, a secondary narrow-beam sonar is employed to correct the elevation information uncertainty of the main wide-beam sonar. Data fusion is undertaken based on geometric constraints related to the sonars installation positions on the vehicle. Such an approach imposes alignment constraints between the different sonar data acquired, which significantly reduces the effective field of view of the main sonar. A visual-sonar odometry system combining monocular camera data with forward looking sonar measurements is presented in [9]. The scale ambiguity problem in monocular visual odometry is solved by generating geometrical constraints on the unknown scale factor based on the acoustic measurements and re-observation of the acoustic features from different viewpoints. Monocular camera depth estimation is also tackled in [10] by projecting measurements from a single-beam echosounder onto the image plane and adjusting the corresponding depth ratio. However, the application scope of visual-sonar systems is limited by the shorter operating range of cameras and water visibility conditions.

In this paper, we introduce a mapping technique that exploits the inversion of the overall rationale governing grid-based methods. Standard approaches employ grid structures to accumulate information directly related to environmental elements. Considering the wide sonar beamwidth and the resulting spatial ambiguity in the recorded acoustic returns, the developed algorithm builds on capturing unoccupied volumes in the environment, resorting to a grid-based approach. Given the range to a recorded acoustic return, the free-space traversed by the emitted sonar beam can be modelled with improved confidence, through the corresponding acoustic echo range and the beam emission angle and aperture characteristics. The boundaries of this free-space representation are subsequently explored to extract a representation of the structures present in the environment. Our approach builds on acoustic images collected from the horizontal plane using a MSIS and corresponding model of the emitted sonar beams to identify free regions in the environment. By not resorting to the combination of multiple sensors, our algorithm is able to preserve the effective field of view and operating range of the MSIS, also avoiding the computational overhead introduced by the secondary sensor. Range extraction is undertaken through a CFAR-based routine and supported by an image pre-processing step, tackling issues related to to multipath interference and acoustic background noise. Resorting to a submapping strategy, map voxels are used to accumulate free-space information. A map of the occupied space is consequently built, as shown in Figure 1, by identifying the limits of the mapped free-space and extracting the corresponding frontier voxels. The work herein extends our previous work in [2] and [11]. We highlight the following contributions in this paper:

1) We introduce a grid-based representation intended to capture unoccupied regions, undertaking map update by modeling the free-space covered by each emitted sonar pulse;
2) We show experimental results for mapping a hydro-electric dam shaft using a ROV equipped with a MSIS.

In what follows, Section II presents an overview of the proposed solution and core concepts associated with it. Section III introduces the overall algorithm structure, providing additional details on each of the developed modules. The real operation scenario used for experimental tests, experimental results and further discussion are presented in Section IV, while Section V summarizes the main conclusions of this work.

II. Problem Statement

We address the problem of mapping a tridimensional environment using an imaging sonar providing ambiguous spatial data. Mapping the environment is one of the critical steps to achieve fully autonomous vehicle navigation. We consider that a vehicle, equipped with a mechanical scanning imaging sonar, insonifies a volumetric region by emitting an acoustic wave. The emitted power follows a pattern that is generally well-characterized by the manufacturer. To reduce the complexity of the corresponding model and to make the problem of mapping tractable, such a pattern is often reduced to a simple shape. In our case, we consider that the sonar emits a pyramidal beam with an elevation angle β and an azimutal angle α, as illustrated in Figure 2. Any *surface* being insonified (inside the pyramidal beam) reflects the acoustic wave back, creating a high intensity measurement on the sonar. By concatenating the measurements, an acoustic image can be obtained. We refer to *surface* as any general object, wall, living creature (etc.) reflecting acoustic waves such as the ones emitted by the sonar. For the type of sensors under consideration, the ambiguity of the sonar data corresponds to the azimutal and elevation angle, that is, it is impossible to discriminate the azimutal and elevation angles of reflecting surfaces from a single beam. Perspective changes are required to produce a more detailed map.

The problem addressed in this paper is the following: to map the surrounding environment in three dimensions using

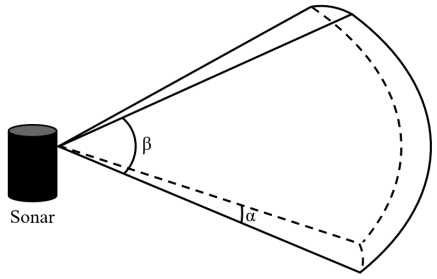

Fig. 2: Illustration of the considered sonar beam model.

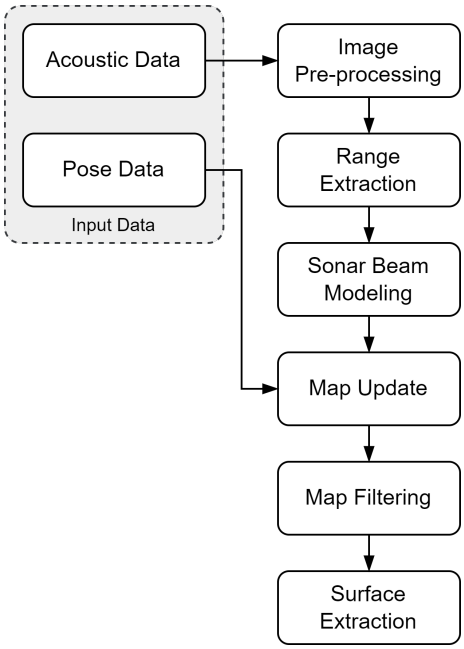

Fig. 3: Block diagram of the mapping pipeline.

a sonar producing an acoustic image with elevation and azimutal ambiguity, while considering background resulting from the coupled structure supporting the sonar.

III. Free-Space Mapping

The mapping strategy builds on the acoustic images collected through the installed sonar. Figure 3 summarizes the proposed mapping pipeline. The delimitation of empty volumes is based on detecting the closest obstacles surrounding the vehicle. Range extraction is supported by an image pre-processing routine tackling errors present in the acquired sonar data, thus reducing the number of outliers in the extracted range information. This information, along with the vehicle pose data, is employed to build three-dimensional models of the respective emitted sonar beams and update the volumetric submaps through beam casting operations. Pose data collection is not further explored in this section, as the localization problem is outside of the scope of this work. Once all measurements are integrated, the free-space frontier voxels are explored, extracting the occupied surfaces.

A. Image Pre-processing

The retrieved acoustic data consists of a series of intensity measurements of the received acoustic echoes resulting from the insonification of water volumes. These are organized in the form of intensity arrays and concatenated to create acoustic images, which results in a representation of the environment considering a polar coordinate system. The final image dimensions depend on the operating range and angular resolution for which the sonar is configured.

Several error sources related to underwater acoustic wave propagation affect image collection, such as acoustic environment noise, multipath effect or secondary reflections. Confined environments are especially prone to the latter two, further increasing the challenges for accurate range extraction. The image pre-processing routine aims at tackling these problems, improving overall image characteristics and mitigating their effect on range extraction.

The acoustic images recovered from the operation site depict a number of high intensity and persistent image artifacts resulting from acoustic reflections on the ROV's body and on the structure to which it was attached during dives, as illustrated in Figure 4. As these elements are of static nature, we address the problem through background subtraction. Their removal is performed through a frame difference approach [12], where an image template I_t of the artifacts is subtracted to the acquired images. This template is built resorting to a temporal median filter [13] and K image samples I^n, pre-retrieved from experimental data obtained during testing sessions:

$$I_t = \text{median}(I^1, I^2, \ldots, I^K). \tag{1}$$

In the case of confined environments, structures as walls may be consistently portrayed in the acquired images and, consequently, incorrectly included in the background template. We employ an additional filtering step that builds on the Density Based Spatial Clustering of Applications with Noise (DBSCAN) algorithm [14] for segmenting artifacts of greater dimensions in the created template. The selected artifacts are evaluated based on the average artifact echo intensity and image spatial distribution, which enables to identify and remove template elements resulting from persistent environmental structures.

Noise filtering is undertaken through image smoothing, resorting to a median filter, and thresholding operations, targeting background and speckle noise. The threshold value is adaptively set using the Otsu's method [15]. A Contrast-Limited Adaptive Histogram Equalization (CLAHE) procedure [16] is employed for improving image contrast, while simultaneously preventing the over-amplification of noise. An illustration of the application of the pre-processing step for images collected from the testing environment is shown in Figure 4.

B. Range Extraction

In sonar applications, object detection is commonly performed through comparison of the received measurements with a predefined threshold [6], [11], [17]. Our approach adopts a two-stage image filtering process, based on thresholding operations employed on the recorded images. First, the Smallest Of Cell Averaging CFAR (SOCA-CFAR) [18] detector is employed for removing denser noise clusters and image artifacts resulting from secondary echoes. The CFAR detector dynamically adjusts a filtering threshold according to the measurement's local noise levels, estimated through a sliding-window technique, ensuring a fixed false alarm probability. The SOCA-CFAR variant is focused on minimizing the effects of interfering artifacts within the sliding-window, allowing to mitigate the interference of secondary echo components. The second stage builds on a multilevel thresholding approach targeting low-intensity pixels. Echo intensity data

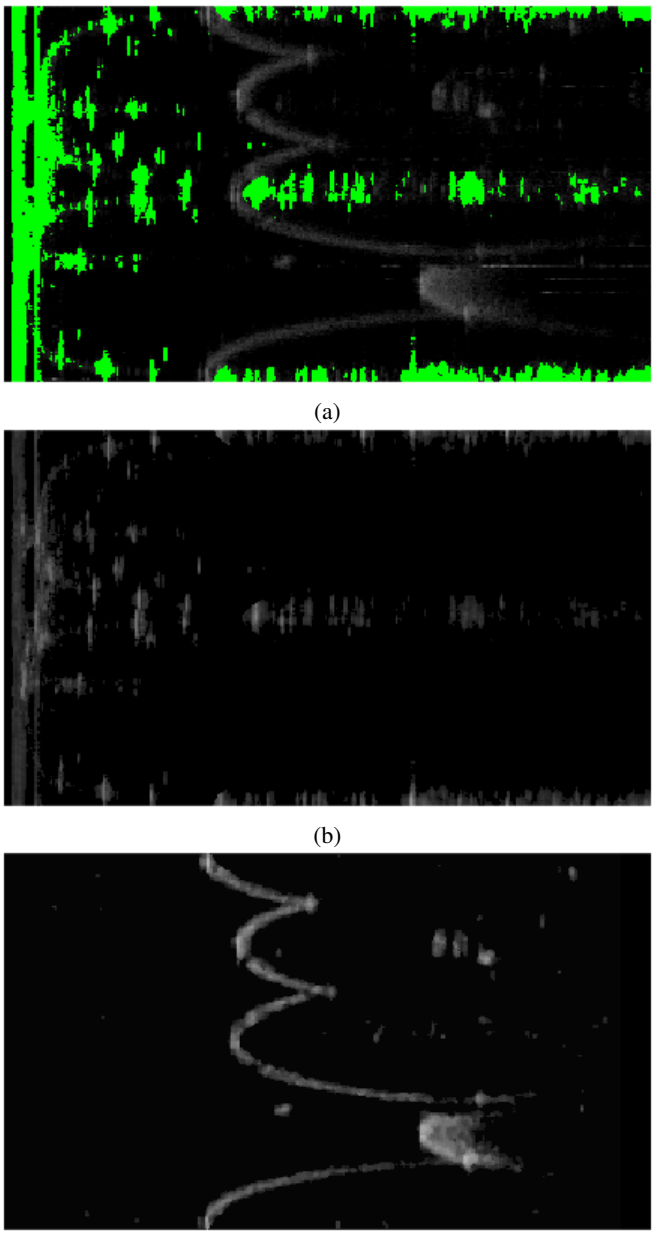

Fig. 4: Application of the image pre-processing step. Static image artifacts highlighted in green. (**a**) Raw sonar image (horizontal plane). (**b**) Background image template. (**c**) Output image.

is partitioned into three classes and sonar returns belonging to the class of lowest intensity are disregarded.

For each array of a filtered image, which is associated to a sonar scanning angle θ_i, the range to the first reflection ρ_i is extracted. We disregard information beyond the closest obstacles as this data may have been corrupted by secondary echoes. Additionally, we undertake a conservative approach for cases where no reflection is detected along an image array, setting the extracted range value to a predefined minimum range value, instead of considering the sonar maximum detection range. This is done to account for a possible inability to correctly capture echo returns from occupied volumes due to viewpoint changes.

C. Submap Representation

Our mapping pipeline relies on a submapping strategy, where the global map M_g is obtained by merging all N local occupancy submaps m_i built from the sonar data. This is done to reduce the computational burden of updating all voxels of the global map at every iteration. Each voxel of a submap is represented by the coordinates of its center of mass, which are expressed with respect to the corresponding local frame of reference r_i, placed at the base pose x_i of the submap. As r_i are globally referenced, we can define the global map M_g as follows:

$$M_g = \{(m_1, r_1), (m_2, r_2), ..., (m_N, r_N)\}. \tag{2}$$

A vacancy score is associated to each voxel, which reflects the probability of the cell being unoccupied.

D. Submap Update and Filtering

The update of local submaps is undertaken taking advantage of the non-zero sonar beamwidth and estimating the volume covered by a single emitted acoustic pulse. Through the sonar's horizontal and vertical aperture characteristics, β and α, respectively, the range information extracted from acoustic images and the vehicle's pose, $X_v = (x_v, y_v, z_v)$, we model the three-dimensional water volume transversed by each pulse until the closest obstacle as follows:

$$X_{free} = \begin{bmatrix} x_{free} \\ y_{free} \\ z_{free} \end{bmatrix} = \begin{cases} \rho_i \cdot \cos(\theta_{h_i}) \cdot \cos(\theta_{v_i}) + x_v \\ \rho_i \cdot \sin(\theta_{h_i}) \cdot \cos(\theta_{v_i}) + y_v \\ \rho_i \cdot \sin(\theta_{v_i}) + z_v \end{cases} \tag{3}$$

, where X_{free} represents the Cartesian coordinates of any point in space classified as empty for a given pair (θ_i, ρ_i), $\theta_{h_i} \in [\theta_i - \frac{\alpha}{2}, \theta_i + \frac{\alpha}{2}]$ and $\theta_{v_i} \in [-\frac{\beta}{2}, \frac{\beta}{2}]$. Through Equation 3, empty-volume models are generated and subsequently employed to update the corresponding submap m_i through beam casting operations, overlapping the centers of mass of each submap voxel with this model. In opposition to common ray casting operations, through the proposed beam casting procedure it is not necessary to discretize the emitted sonar beam, tackling the problem of loss of resolution with increasing range and ensuring that a voxel is only updated once for each range measurement. A tolerance value is considered, contemplating cases where the voxel is intersected by the model created but not its center of mass. The vacancy scores reflect the number of times a voxel is intersected by empty-volume models.

Once every acoustic image is processed, the global map is assembled by merging all submaps through the local reference frames r_i. A filtering routine is introduced that classifies voxels as empty if the corresponding vacancy score is over a user-defined threshold. Otherwise, the voxel is disregarded.

E. Surface Extraction

The extraction of the surface is achieved by detecting the frontier of the empty volume, as a whole. By taking advantage of the voxel map representation, we start finding the neighborhood of a given voxel i based on the distance to the respective position p_i. Any voxel j at a distance $||p_j - p_i||_\infty \leq d_r$ is considered a neighbour of voxel i, where d_r is the voxel map resolution. Note that, in three dimensions, the number of neighbours always equals $n_N = 3^3 - 1 = 26$. Then, we find the voxels that are at the frontier of the empty volume, referred to as *frontier voxels*, by searching for voxels that contain less than n_N neighbours that are considered empty. The surface is finally composed of the entire set of *frontier voxels*.

IV. Results and Analysis

In this section we introduce a thorough analysis of the performance of the proposed system, supported on illustrative results. Experimental tests were undertaken making use of the MATLAB R2023a software.

A. Experimental Setup

The experiments performed with the proposed mapping system resort to a dataset collected through data surveys conducted in a hydroelectric dam. The data was collected along a vertical profile of the ROV, with it in a fixed horizontal position that was guaranteed by a mechanical structure. This structure is responsible for controlling the descent/ascent of the vehicle, at constant velocity. Fixing the horizontal position and attitude removes the horizontal localization problem, which is beyond the scope of this paper. The profile was performed in a chamber conducting to the penstock and in the penstock itself. Figure 5 shows a lateral view of the chamber and of the penstock, along with the profile performed by the sonar during the descent/ascent. Note that the overall structure presents a constant width of $6m$.

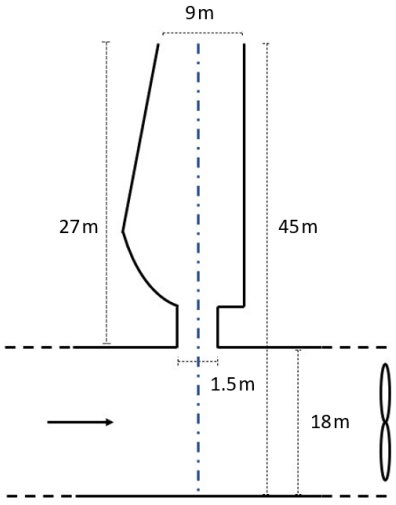

Fig. 5: Lateral section cut of the chamber and penstock of the reservoir dam where data was acquired. The blue point-dashed line shows the vertical profile for data acquisition.

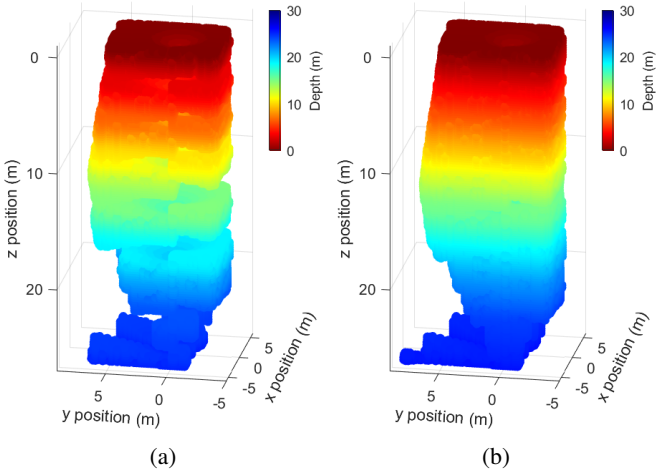

Fig. 6: Illustration on the map update process with depth-based color coding. (**a**) Free-space representation using 10 images. (**b**) Free-space representation using 20 images.

The gain and the range of the sonar were adjusted manually during the operation to guarantee that surrounding surfaces were observed. The connection between the chamber and the penstock is done through a narrow rectangular passage, which we refer to as *connection duct*.

Data collection was undertaken resorting to a ROV equipped with a Tritech Micron MSIS and a depth sensor. The sonar is mounted with the rotation axis parallel to the up/down axis, enabling to collect acoustic images of the horizontal plane. The depth sensor enables to extract the vehicle's vertical position and, consequently, to fully characterize its motion during the experiment, since the horizontal position and attitude do not vary. The constructed dataset portrays a single dive-resurface sequence. The ROV is lowered from the chamber until the middle of the penstock and brought back up.

B. Experimental Results

Despite the imbalance in the collected data and the speed at which the ROV's descent and ascent were performed, that resulted in a reduced number of images being collected from within the chamber, the proposed mapping pipeline is able to provide a consistent representation of this section. It should be highlighted the system's ability to coherently capture the oblique wall, as the surface inclination elongates the corresponding acoustic representation, further contributing for the associated perceptual ambiguity. The reduced inclination of segments of the chamber, which prevents to fully capture the returning acoustic echoes, and the motion of the vehicle induce distortions in the retrieved acoustic images. By considering the three-dimensional model of the transversed empty regions, the map update process takes into account information not directly represented in the images, allowing to extrapolate information about areas not represented in the two-dimensional cross-section and correct possible outliers. Figure 6 illustrates such capability. It is also possible to observe the method's ability to capture more

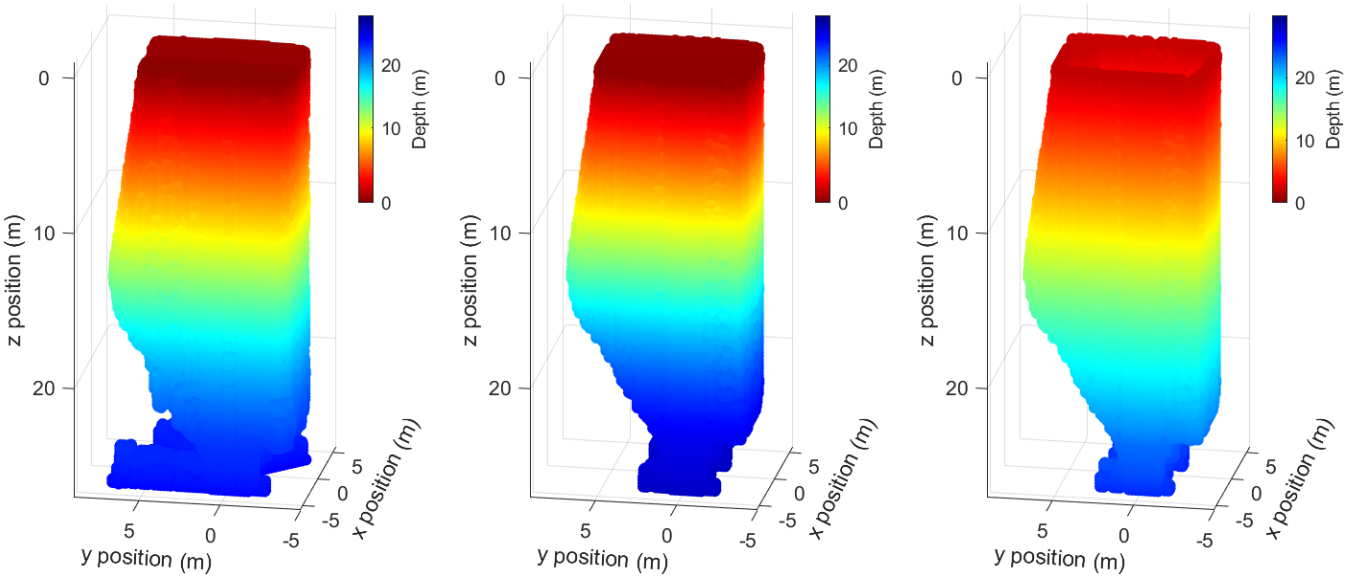

Fig. 7: Example results on surface map extraction, with depth-based color coding. (**a**) Free-space representation after processing all acoustic images from within the chamber section. (**b**) Chamber section free-space representation after submap filtering. (**c**) Extracted occupied surface map of the chamber section.

complex details, as in the case of the narrow connection between the chamber and the penstock.

Regarding the penstock, the representation obtained is significantly affected by the lack of motion along the horizontal plane. The approach is able to correctly capture the lateral walls, from which constant sonar returns were collected, but, the inability to insonify other structures results in map update being consistently undertaken resorting to the predefined minimum range value, leading to a contraction of the duct representation along the y axis. In spite of the absence of horizontal motion, the top surface of this section is partially represented.

Figure 7 provides a detailed representation of the surface map building process, focusing the chamber section. These results illustrate the ability of the voxel filtering step to tackle the contributions of range extraction outliers. These are expected to generate low vacancy score increments in map voxels, thus the efficiency of the filtering step in improving the the accuracy of the surface representation and the level of detail of the final map. Taking into account Figure 5, Table I introduces the estimated dimensions of the chamber. A maximum error of 12% was registered, which further supports the achievable mapping accuracy of the presented algorithm.

	Chamber Height	Chamber Entry Length	Chamber Width	Connection Duct Width
Ground-truth (m)	27.00	9.00	5.00	1.50
Estimated (m)	26.10	8.80	5.60	1.40
Relative Error $(\%)$	3.33	2.22	12.00	6.67

TABLE I: Results on estimated dimensions of the chamber and connection duct.

V. Conclusion

This paper introduced a grid-based approach for underwater mapping through acoustic images obtained from an imaging sonar, tackling the perceptual ambiguity problem characteristic of wide-aperture sonars. Building on the modeling of the unoccupied water volume covered by the emitted acoustic pulses, a volumetric submap-based representation of the free-space is generated and an occupied surface representation is extracted by exploring the free-space frontier voxels. Range extraction is undertaken through a SOCA-CFAR application and supported by an image preparation step, aimed at tackling common problems in acoustic imagery. The developed system was analysed resorting to real data collected from a hydroelectric dam. The results presented assert for the ability of the method to create consistent representations of the operation environment. Note that the considered confined environment is especially prone to acoustic noise and multiple reflections from the surrounding structures, raising the complexity of the task at hands.

In the proposed approach, map update is performed identically for each voxel selected through beam casting. Making the vacancy score update dependent of the elevation and azimutal angle information, reflecting the corresponding uncertainty, may enable to filter additional outliers in the free-space representation built. Additional future work will focus the integration of the developed mapping pipeline into a Simultaneous Localization and Mapping (SLAM) framework. Whether to address the localization part of the SLAM problem based on the free-space representation or the occupied surface representation is a key aspect to tackle.

REFERENCES

[1] J. Wang, S. Bai, and B. Englot, "Underwater localization and 3d mapping of submerged structures with a single-beam scanning sonar," in *2017 IEEE International Conference on Robotics and Automation (ICRA)*. IEEE, 5 2017, pp. 4898–4905.

[2] P. M. Goncalves, B. M. Ferreira, J. C. Alves, and N. A. Cruz, "Image segmentation and mapping in an underwater environment using an imaging sonar," in *OCEANS 2022, Hampton Roads*. IEEE, 10 2022, pp. 1–8.

[3] H. Rohling, "Radar cfar thresholding in clutter and multiple target situations," *IEEE Transactions on Aerospace and Electronic Systems*, vol. AES-19, pp. 608–621, 7 1983.

[4] A. Nunes, A. R. Gaspar, and A. Matos, "Occupancy grid mapping from 2d sonar data for underwater scenes," in *OCEANS 2021: San Diego – Porto*, vol. 2021-September. IEEE, 9 2021, pp. 1–8.

[5] A. Hornung, K. M. Wurm, M. Bennewitz, C. Stachniss, and W. Burgard, "Octomap: an efficient probabilistic 3d mapping framework based on octrees," *Autonomous Robots*, vol. 34, pp. 189–206, 4 2013.

[6] P. V. Teixeira, M. Kaess, F. S. Hover, and J. J. Leonard, "Underwater inspection using sonar-based volumetric submaps," in *2016 IEEE/RSJ International Conference on Intelligent Robots and Systems (IROS)*, vol. 2016-November. IEEE, 10 2016, pp. 4288–4295.

[7] B. Ho, P. Sodhi, P. Teixeira, M. Hsiao, T. Kusnur, and M. Kaess, "Virtual occupancy grid map for submap-based pose graph slam and planning in 3d environments," in *2018 IEEE/RSJ International Conference on Intelligent Robots and Systems (IROS)*. IEEE, 10 2018, pp. 2175–2182.

[8] H. Joe, J. Kim, and S.-C. Yu, "Sensor fusion-based 3d reconstruction by two sonar devices for seabed mapping," *IFAC-PapersOnLine*, vol. 52, pp. 169–174, 2019.

[9] D. Yang, H. Ai, J. Liu, and B. He, "Absolute scale estimation for underwater monocular visual odometry based on 2-d imaging sonar," *Measurement*, vol. 190, p. 110665, 2 2022.

[10] M. Roznere and A. Q. Li, "Underwater monocular image depth estimation using single-beam echosounder," in *2020 IEEE/RSJ International Conference on Intelligent Robots and Systems (IROS)*. IEEE, 10 2020, pp. 1785–1790.

[11] A. J. Oliveira, B. M. Ferreira, and N. A. Cruz, "Real-time wall identification for underwater mapping using imaging sonar," in *OCEANS 2022, Hampton Roads*, vol. 2022-Octob. IEEE, 10 2022, pp. 1–7.

[12] Y. Benezeth, P. Jodoin, B. Emile, H. Laurent, and C. Rosenberger, "Review and evaluation of commonly-implemented background subtraction algorithms," in *2008 19th International Conference on Pattern Recognition*. IEEE, 12 2008, pp. 1–4.

[13] W. Liu, Y. Cai, M. Zhang, H. Li, and H. Gu, "Scene background estimation based on temporal median filter with gaussian filtering," in *2016 23rd International Conference on Pattern Recognition (ICPR)*, vol. 0. IEEE, 12 2016, pp. 132–136.

[14] E. Schubert, J. Sander, M. Ester, H. P. Kriegel, and X. Xu, "Dbscan revisited, revisited: Why and how you should (still) use dbscan," *ACM Transactions on Database Systems*, vol. 42, pp. 1–21, 8 2017.

[15] N. Otsu, "A threshold selection method from gray-level histograms," *IEEE Transactions on Systems, Man, and Cybernetics*, vol. 9, pp. 62–66, 1 1979.

[16] L. Zheng, H. Shi, and S. Sun, "Underwater image enhancement algorithm based on clahe and usm," in *2016 IEEE International Conference on Information and Automation (ICIA)*. IEEE, 8 2016, pp. 585–590.

[17] D. Ribas, P. Ridao, J. Neira, and J. Tardos, "Slam using an imaging sonar for partially structured underwater environments," in *2006 IEEE/RSJ International Conference on Intelligent Robots and Systems*. IEEE, 10 2006, pp. 5040–5045.

[18] M. Sahal, Z. A. Said, R. Y. Putra, R. E. A. Kadir, and A. A. Firmansyah, "Comparison of cfar methods on multiple targets in sea clutter using spx-radar-simulator," in *2020 International Seminar on Intelligent Technology and Its Applications (ISITIA)*. IEEE, 7 2020, pp. 260–265.